Effects of unreconstructed and reconstructed polar surface terminations on growth, structure, and magnetic properties of hematite films

S. H. Cheung, A. Celik-Aktas, P. Dey, K. Pande, M. Weinert, B. Kabius, D. J. Keavney, V. K. Lazarov, S. A. Chambers, and M. Gajdardziska-Josifovska

Phys. Rev. B **85**, 045405 — Published 5 January 2012

DOI: 10.1103/PhysRevB.85.045405

Effects of Unreconstructed and Reconstructed Polar Surface Terminations on Growth, Structure, and Magnetic Properties of Hematite Films

S. H. Cheung[1,*], A. Celik-Aktas[1,**], P. Dey[1,***], K. Pande [1], M. Weinert[1], B. Kabius[2†],

D. J. Keavney[3], V. K. Lazarov[4††], S. A. Chambers[5] and M. Gajdardziska-Josifovska[1‡]

[1]Department of Physics and Laboratory for Surface Studies, University of Wisconsin-Milwaukee, P. O. Box 413, Milwaukee, WI 53201, USA

[2] Environmental Molecular Science Laboratory, Pacific Northwest National Laboratory, P. O. Box 999, Richland, WA 99352

[3] Advanced Photon Source, Argonne National Laboratory, Argonne, IL 60439, USA

[4] Department of Materials, Oxford University, Parks Road, Oxford OX1 3PH, UK

[5] Chemical and Materials Science Division, Pacific Northwest National Laboratory, P. O. Box 999, Richland, WA 99352

Abstract

The effects of polar surface stabilization mechanisms on the film growth, phase composition, surface and interface structure, and magnetic properties are explored for polar oxide interfaces formed by the epitaxial growth of hematite films on magnesia and alumina single crystals. Growth of α-Fe_2O_3(0001) on the ($\sqrt{3}\times\sqrt{3}$)R30° and (2×2) reconstructed MgO(111) surfaces results in formation of a self-organized Fe_3O_4(111) interfacial nano-buffer that persists after growth. The interface magnetite-like phase is absent from the hematite films formed on hydrogen-stabilized unreconstructed MgO(111)-(1×1) and on Al_2O_3(0001)-(1×1) surfaces under equivalent conditions. This study suggests that in addition to the customary strain, spin, and band-gap engineering, control of surface polarity stabilization could also be important for electronic and magnetic device engineering.

Curent addresses: *Micron Technology, 8000 S Federal Way, Boise, ID 83716-9632, USA ; **Department of Engineering Physics, Faculty of Engineering, Ankara University, TR-06100 Besevler-Ankara, Turkey; *** Department of Applied Physics, University of South Florida, Tampa, FL- 33620; †Pacific Northwest National Laboratory, Interfacial & Nanoscale Science Facility, P.O. Box 999, Richland, WA 99352, USA; †† Department of Physics, University of York, Heslington, York, YO10 5DD,U.K.

†Communicating author: mgj@uwm.edu, fax: (414) 229 5589; tel. (414) 229 4965.

Introduction

Ionic metal oxide surfaces fall into three basic categories: neutral, charged, and polar [1]. By definition, bulk-terminated polar oxide surfaces have a net charge in each plane and a net dipole moment in the repeat unit perpendicular to the surface. The stability of polar oxide surfaces has long been a problematic question, as discussed in several books and reviews [2-6]. The structure of polar oxide surfaces appears to be determined by the tendency to cancel, or at least minimize, the net electric dipole moment perpendicular to the surface. Different surface stabilization models have been proposed and studied, with reconstruction [7-14] and hydrogen adsorption [12-17] being the two relevant mechanisms for the present study of growth on the prototypical MgO(111) polar oxide surface with the rock-salt structure. This surface has been shown to display ($\sqrt{3}\times\sqrt{3}$)R30° [7,10,11,13] and (2×2) [10,12,13] surface reconstructions upon high temperature annealing, and (1×1)-OH termination when prepared at lower temperatures [13,16,17]. Water evolution appears to play an important role in the structures of the reconstructed surfaces even when these are prepared in UHV [14].

The question of the stability of polar interfaces is closely related to that of polar surfaces, both by the physics of the problem, and also because polar interfaces can be created by film growth on polar surfaces. It is reasonable to hypothesize that: 1) The polar surface stabilization solution would be perturbed by each new layer of the growing film, resulting in atomic and electronic structures that would likely be defined by the need to minimize, in a dynamic way, the net dipole of the film/substrate system within its growth environment, on the way to a static terminal-state solution; 2) The system dipole minimization might be accomplished by structural and electronic changes at the solid/solid interface, the film surface, and/or within the film; 3)

Different initial surface stabilization mechanisms of the polar oxide substrate could effect the structure and properties of the final hetero-interface polar oxide system in different and observable ways.

Initial investigation of growth of polar magnetite (Fe_3O_4) films on the hydrogen stabilized unreconstructed MgO(111) surface [18,19] has shown marked differences in comparison with magnetite growth on the corresponding neutral MgO(001) surfaces [20,21] and on metal Pt(111) surfaces [22], suggesting that the substrate surface polarity drives phase separation with nucleation of Fe nanocrystals. Phase separation was also found in the growth of iron oxides on the corundum structure α-Al_2O_3(0001) substrates [23], with single phase growth of magnetite achieved under much more oxidizing conditions than those needed for single-phase growth on the neutral MgO(001) surface. These results inspire the first question for the present study: Is it possible to grow the terminal oxidation phase of iron (i.e., hematite α-Fe_2O_3(0001) film) on the strongly polar MgO(111) surfaces?

The second question this study seeks to address is whether or not the surface stabilization mechanism for a polar oxide substrate has any noticeable effect(s) on the growth, structure, and properties of the polar hematite films. Prior studies of GaN growth on the unreconstructed MgO(111)-(1×1)-OH terminated surface revealed that the higher-energy GaN(111) cubic polymorph can be stabilized when the surface hydrogen is replaced by nitrogen in the initial stages of growth. In contrast, hexagonal GaN(0001) nucleates under identical conditions when growth is initiated with gallium on the hydrogen terminated surface [24]. The present study compares and contrasts the structure and magnetic properties of iron oxide films grown under equivalent highly-oxidizing conditions on unreconstructed MgO(111) and Al_2O_3(0001), and on reconstructed MgO(111) surfaces.

Materials background

The controlled growth of hematite and magnetite films has been a subject of intense studies inspired by their many technological applications in catalysis, gas sensing, sequestration of toxic metals, and magnetic devices (e.g., reviews [25-27] and references therein). Bulk hematite is a high Néel temperature (953K) canted antiferromagnetic oxide, with 2.2 eV band gap, with potential uses in exchange-biased devices and sensors to pin the magnetization of an adjacent ferromagnetic layer. Magnetite is a high Curie temperature (854K) ferrimagnet that is of interest as a source of spin-polarized electrons. The bulk spin polarization, as estimated by spin-polarized photoemission, is ~50-65% for Fe_3O_4(001) epitaxial films grown on MgO(001) [28,29]. In combination with a tunneling barrier from an insulating oxide such as MgO or Al_2O_3, magnetite and hematite are of interest for spintronic devices such as magnetic tunnel junctions [30]. Hematite is also studied as promising photoanode material for conversion of sunlight into hydrogen as clean source of renewable energy ([31] and references therein).

This combination of materials is also of great interest due to the close lattice match that allows controlled epitaxial growth of the active layers. Bulk hematite (α-Fe_2O_3) has the rhombohedral corundum structure (bulk unit cell dimensions: a=0.504nm and c=1.375nm) with a close-packed hexagonal O^{2-} sub-lattice and with Fe^{3+} in distorted oxygen octahedral sites (Fig. 1a). In the polar <0001> direction the corundum structure of α-Fe_2O_3 (and α-Al_2O_3) consists of alternating planes of oxygen mono-layers, with three O^{2-} anions per unit cell, and metal bi-layers with one Fe^{3+} (Al^{3+}) cation per each layer. The surface is charged but non-polar when bulk-terminated with a cation monolayer; it is charged and polar when terminated with oxygen or a

complete cation bi-layer. The semantics can be confusing because the cation bi-layer is called a monolayer in some references; hence, half a monolayer is needed for a non-polar termination.

Magnetite (Fe_3O_4) has the cubic inverse spinel structure (a=0.840nm) with oxygen forming an fcc sub-lattice and with Fe^{2+} cations in octahedral sites and Fe^{3+} in octahedral and tetrahedral sites. The {100} and {111} faces of magnetite are polar where, in the <111> direction, magnetite consists of close-packed oxygen monolayers, separated by alternating iron monolayers with Fe^{3+} and tri-layers with Fe^{2+} Fe^{3+} Fe^{2+} stacking, as illustrated in Fig. 1b. Bulk maghemite (γ-Fe_2O_3), while sharing the same stoichiometry as the hexagonal hematite, is ferrimagnetic due to its cubic structure that shares many similarities with magnetite shown in Fig. 1b, with all or most Fe in the trivalent state. It has a cubic unit cell (a=0.824nm) which contains 32 O^{2-} ions, 64/3 Fe^{3+} ions and 7/3 vacancies. The cations are distributed randomly over the 8 tetrahedral and 16 octahedral sites, while the vacancies (which are also randomly distributed) are confined to the octahedral sites [32]. Consequently, the {111} planes of maghemite are also polar.

In addition to externally imposed stoichiometry (i.e., through control of cation and anion delivery rates at the growth surface), the phase composition of iron oxide films is also affected by kinetics, thermodynamics, and elastic constraints. Therefore, controlled growth of iron oxides of desired phase composition is no small feat [25-27].

Magnesia (MgO) has the cubic rock-salt structure (a=0.421nm) typical for extremely ionic materials, with fcc Mg and O sub-lattices. Its polar <111> direction consists of alternating close-packed layers of Mg^{2+} and O^{2-} as shown in Fig. 1c. The small in-plane lattice mismatch between a relaxed α-Fe_2O_3(0001) film and α-Al_2O_3(0001) substrate (5.32%) or MgO(111)

substrate (-2.25%), and between Fe_3O_4(111) film and MgO(111) substrate (-0.24%) is attractive for applications in electronic and magnetic devices.

Experiment

Iron oxide films were grown on magnesia and alumina substrates by oxygen plasma-assisted molecular beam epitaxy (OPA-MBE) in a custom built system [26] designed specifically for oxide growth. Films were grown with the same iron flux and oxygen partial pressure on unreconstructed and reconstructed MgO(111) substrates, and on unreconstructed Al_2O_3(0001) substrates, as summarized in Table 1. During growth of all samples, an e-beam evaporated Fe source was used, with the metal beam flux of ~0.1 Å/s monitored and controlled by atomic absorption spectroscopy. Plasma discharge activated oxygen gas was generated at a constant partial pressure of $\sim 2\times10^{-5}$ torr.

Epi-polished single crystal MgO(111) and Al_2O_3(0001) surfaces (10mm x 10mm x 0.5mm) were cleaned with acetone and isopropanol. The magnesia crystals were annealed in a tube furnace of flowing oxygen at 800°C (for 1 hr) and 1100°C (3 hrs) for the preparation of unreconstructed (MU) and reconstructed (MR) surfaces, respectively. Preparation of the unreconstructed single crystal alumina (AU) substrates did not require initial annealing. All three substrate types were treated in a UV ozone cleaner immediately prior to insertion in the ultrahigh vacuum growth chamber, and then exposed *in situ* to activated oxygen (55mA at 2×10^{-5}torr O_2 partial pressure) at room temperature for times between 30 min (AU and MR substrates) and 1 hr (MU) to remove carbon. Additional *in situ* annealing at ~500°C for 20 minutes was performed

for the MR substrates. All films were grown under nominally identical iron flux, oxygen partial pressure and substrate temperature conditions.

In situ characterization of the substrate and film surfaces was performed using reflection high-energy electron diffraction (RHEED) and x-ray photoelectron spectroscopy (XPS). RHEED was used to verify the substrate quality and surface reconstruction prior to growth, and to monitor the film crystallinity and surface morphology during and after growth. The composition and Fe charge state of each film surface was measured in an appended XPS chamber using a Gammadata/Scienta SES 200 photoelectron spectrometer with a monochromatic Al Kα x-ray source.

Upon removal from ultrahigh vacuum, a Lakeshore 7400 Vibrating Sample Magnetometer (VSM) was used to characterize the magnetic properties of the films at room temperature. The film crystal structure was characterized with high-resolution x-ray diffraction (XRD) using a Philips X'Pert four-circle diffractometer, as well as with selected area diffraction (SAD) and high-resolution transmission electron microscopy (HRTEM) performed in a Hitachi H-9000NAR electron microscope operated at 300 keV. Cross-sectional samples were prepared in two mutually perpendicular azimuths with tripod mechanical polishing followed by low-angle Ar ion milling methods. The film and interface morphology was studied by bright field transmission electron microscopy (TEM) in the same instrument, and the film surface morphology was studied by atomic force microscopy (AFM) using a Digital Instruments Nanoscope IIIa multimode scanning probe microscope with Si cantilevers. The film composition was characterized by electron energy loss spectroscopy (EELS) in a Tecnai F20ST TEM/STEM analytical microscope operated at 200 keV in an energy filtered TEM mode. X-ray magnetic circular dichroism (XMCD) and x-ray absorption spectroscopy (XAS) synchrotron studies were

performed at beamline 4-ID-C at the Advanced Photon Source to obtain additional magnetic and compositional information about the buried substrate-film interface.

Results and Discussion

A. Macroscopic Film Structure and Magnetic Properties

Magnetic hysteresis loops obtained by VSM measurements are shown in Fig. 2. In all cases the predominantly antiferromagnetic films possess non-zero coercivity, indicating the presence of a small ferro(ferri)magnetic component in films grown on unreconstructed surfaces (MU, AU) and markedly higher saturation magnetization and coercivity for films grown on reconstructed surfaces (MR). The magnetic properties of these films are summarized in Table 2. The thickness normalized saturation magnetization in Fig. 2 is larger by a factor of 6 in MRc than MUc samples, and the coercivity by a factor of 3. In all three film types the ratio of the remanence to saturation magnetization (M_r/M_s) falls within the (~0.05-0.5) range typical for pseudo-single domain (PSD) magnetite, as does the ratio of the field to remove remanence to the coercive field (H_{cr}/H_c: ~1.5-4.0 PSD) [32].

The above property measurements lend the first evidence in support of the hypothesis that "different initial surface stabilization mechanisms of the polar oxide substrate could affect the structure and properties of the final hetero-interface polar oxide system in different and observable ways". It is important to find out if this difference in magnetic properties is driven by differences in structure and/or composition. Three iron-based structures would give hysteresis loops with substantial coercivity and saturation magnetization: Fe metal, Fe_3O_4, and/or γ-Fe_2O_3.

We next present the macroscopic structural characterization by X-ray diffraction to probe if any of these magnetic phases are present.

In Figure 3 we compare the XRD intensity profiles of films grown on reconstructed (MR) and unreconstructed (MU) magnesia showing that both films can be indexed as hematite growing with its (0001) planes parallel to the magnesia (111) polar planes. While in other systematic studies with lower oxygen pressures we could detect epitaxial Fe (110), Fe_3O_4(111) and γ-Fe_2O_3(111) film reflections, these are absent from Figure 3 demonstrating that the films are α-Fe_2O_3(0001) within the XRD detection limit. Hence, it is not possible to explain the large differences in magnetic properties by macroscopic differences in the film crystal structure.

XAS and XMCD studies were undertaken to study the composition and magnetic properties of the films in search of an explanation for the vastly different VSM results. The Fe L edge XAS data (Fig. 4a) are indicative of Fe^{3+} as expected for Fe_2O_3. The very weak XMCD signal (bottom curves in Figs. 4a), calculated as the difference between the absorption of x-rays with left and right circular polarization, is also consistent with the antiferromagnetic nature of the dominant hematite phase. The weak magnetic signal (~0.7% of XAS intensity for MUc, ~0.6% for MRc, and ~4.5% for AUc), recorded with the samples in remanence, shows small but potentially significant differences. A triplet of lines, indicated as features a, b, and c in the XMCD AUc spectrum, has peak height ratios representative of maghemite (a<c for bulk γ-Fe_2O_3). The XMCD signal is smaller for the films grown on magnesia, yet the discernible triplet in the MUc sample has a reversed peak ratio suggestive of a small magnetite-like component (a>c in bulk Fe_3O_4). The line shape in MRc is different from the known maghemite and magnetite line shapes, but the signal is too small to allow definite identification. Due to strong self-absorption effects at the Fe L resonances, these data were taken via electron yield detection,

which is sensitive to the top ~5 nm of the film, including any changes that might be introduced by transport through air. It will be shown later, however, that the same Fe^{3+} result was obtained from in-situ XPS (Fig. 5) of the as-grown film surfaces measured under ultrahigh vacuum, and is therefore unlikely to be due to post-growth exposure to air.

The oxygen K-edge XAS data (Fig. 4b) were recorded in fluorescence yield, providing increased depth sensitivity (top ~100 nm). All films show two sharp features (a,b), derived from mixing of the O 2p and Fe 3d states. The films on unreconstructed magnesia and alumina have similar a:b ratios, but the film on the reconstructed magnesia surface shows markedly lower a:b intensity ratio, suggestive of a buried interface layer with different Fe/O stoichiometry. The broader features (c,d) at higher energy, due to the more diffuse 4s and 4p states, are also visible on all three films with some subtle differences in intensity and position. The highest energy features (e, f, g) differ substantially between the films on alumina (only f and g peaks present in AUc) and magnesia (e peak is present in the MU and MR films, but small f and g contributions are seen only in MUc). These features likely arise from multiple scattering contributions, thus they point to significant differences in the oxygen local environment between the alumina and magnesia-grown films.

B. Surface Composition, Structure and Morphology

In-situ XPS Fe 2p spectra from the as-grown films are consistent with Fe^{3+} (Fig. 5), indicative of Fe_2O_3 formation. Upon correction for charging effects using the O 1s peak, the experimentally measured Fe peak positions are in close agreement with the bulk hematite values of 711 eV for Fe $2p_{3/2}$ and 719 eV for the satellite peak. While phase separation with formation

of Fe^0 and Fe^{2+} valence states had been observed in iron oxide films grown on polar magnesia [18] and alumina [23] surfaces, the top regions of the films appear to be pure Fe^{3+}, presumably because of the strongly oxidizing conditions. O 1s XPS (not shown here) display symmetric peaks indicative of lattice oxygen and no surface OH, which typically appears as a shoulder ~1.5 eV to higher binding energy. Substrate cation outdiffusion was of concern at the higher growth temperatures (250-500°C) needed to form Fe_2O_3. For example, Mg segregation to the film surface has been found for γ-Fe_2O_3 grown on neutral MgO(001) substrates [33-36], but no Al has been detected at surfaces of α-Fe_2O_3 films grown under similar conditions on Al_2O_3(0001) substrates [36-38]. In the present study we do not find detectable amounts of Al or Mg at the surface of any of our films.

Figure 6 shows *in-situ* RHEED patterns from magnesia and alumina substrates upon surface preparation for growth (top row) and from respective film surfaces upon completion of OPA-MBE growth (bottom row). The substrate patterns are streaky in both MgO cases, indicative of flat surfaces, and the sharpness of the streaks is indicative of extended reconstruction domains. The spotty nature of most film patterns is indicative of development of surface roughness in the films; the smoothest surface being obtained for the MRc film grown on the reconstruction stabilized MgO(111) surface (Fig. 6b). All film surfaces are consistent with an unreconstructed α-Fe_2O_3(0001)-(1×1) structure. Referring back to the atomic models in Fig. 1, it is evident that the hematite (0001) plane fits on the alumina (0001) plane without any rotation (Fig. 1a), but it fits on the magnesia (111) plane with a 30° rotation and $\sqrt{3}\times\sqrt{3}$ relationship between the surface unit cells (Fig. 1c). This orientation relationship produces the same number of RHEED rods for the alumina (Fig. 6c), the reconstructed MgO(111)-($\sqrt{3}\times\sqrt{3}$)R30° substrate (Fig. 6b) and the hematite films. The fit to the unreconstructed MgO(111)-(1×1) is via overlap of

its (11) rod with the hematite (30) rod, with the (10) and (20) rods trisecting the distance (Fig. 6a). If the films were terminated with epitaxial magnetite or maghemite, their (11) rods would bisect the distance to the magnesia (11) rods, but this is not observed in the experimental RHEED patterns, nor in their intensity profiles. The in-plane (*hk*) intensity profiles (Fig. 6d), obtained by mirror averaging of the above RHEED patterns around the (00) specular reflection and by averaging over ~6 nm^{-1} along the l direction of each (*hk*) rod, indicate that the film on alumina is compressed compared to the films on magnesia. The bulk MgO d_{220} = 0.1488 nm lattice spacing was used for calibration of the RHEED patterns, corresponding to the first rod of the MgO(111)-(1x1) pattern. This substrate reflection is close to the third order hematite film rods based on epitaxial constraints; experimentally we find 0.140 nm for MUc, 0.141 nm for MRc, and 0.136 nm for AUc, smaller by 3.3%, 2.9%, and 6.1% respectively from the closest bulk α-Fe_2O_3 lattice spacing of 0.1452 nm.

In-situ x-ray reflectivity studies by Lee at al. [39] have found initially flat but compressed hematite films (RMS ~0.3-0.4 nm for thicknesses less than ~16 nm), that roughen abruptly as they relax (RMS increases to ~1.0 nm for film thicknesses between 16 and 21 nm), followed by slower roughening rate as hematite dc sputtering growth continues on alumina (0001) substrates. Weiss and Ritter [40] have reported vertical roughness ranging from 3 to 15 nm in hematite films grown by metal monolayer deposition and oxidation on Pt(111) surfaces. In comparison, quantitative AFM investigations of our OPA-MBE grown hematite film surfaces find RMS roughness that is similar for films on hydrogen stabilized magnesia and alumina (~1.2 nm), and somewhat smaller on the reconstructed magnesia (~0.9 nm), consistent with the RHEED observations in Fig 6. In all cases the film surfaces do not display signs of faceting into larger angle neutral faces.

Combined with the XAS and XPS data presented above, the RHEED data confirms that the surface structure of all films is hematite, and that the observed differences in magnetic properties of the films are not likely due to composition, structural, or morphological differences in the near-surface region. We turn our attention, therefore, to the substrate-film interfacial region as a possible explanation for the observed changes in magnetic properties.

C. Interface Composition, Structure and Morphology

The low magnification bright-field TEM image of an MU film (Fig. 7) is recorded in a weakly diffracting condition for the MgO substrate, emphasizing the difference in mass thickness between the substrate and the film. Similar imaging conditions have been used previously [18] to visualize phase separation within magnetite films grown on unreconstructed MgO(111) surfaces where Fe nanocrystals were detected through their higher mass density contrast at the interface and in the film. Such metallic nanocrystals, however, are absent from all films studied here. The film thickness is uniform, except for the minor surface roughness, but the actual average thickness (112 ± 3 nm) measured by TEM is drastically smaller than the nominal thickness (200 nm) predicted during growth, which was based on calibrations for Fe_2O_3 growth on alumina (0001) and on neutral magnesia (001) surfaces. The difference between the actual and nominal thickness, as well as the average surface corrugations measured by TEM, appears to depend strongly on the polar substrate stabilization mechanism. For the film grown on reconstructed magnesia (MRc) the actual thickness (70 ± 1 nm) is closer to the nominal thickness (80 nm). The above pattern regarding film thickness is also seen for the start-stop films on magnesia substrates.

Figure 8 shows electron diffraction patterns from cross-sectional samples of hematite films grown on the unreconstructed (a; MUc) and reconstructed (b; MRc) polar magnesia surfaces. These diffraction patterns are recorded from selected area sample regions that are ~500 nm in diameter, with the MgO(111) substrate oriented in a [11-2] zone. The magnesia and hematite reflections are clearly visible in both patterns, as denoted by their unit cells. The orientation relationship between the substrate and the dominant hematite film phase can be summarized as <0001>α-Fe_2O_3||<111>MgO; <11-20>α-Fe_2O_3||<11-2>MgO and <1-100>α-Fe_2O_3||<1-10>MgO; in the case of hematite grown on alumina, all directions in both corundum structures are in alignment. These 3D relationships are consistent with the 2D in-plane orientations seen at the hematite film surface by RHEED (Fig. 6), and the 1D growth direction orientation seen by XRD (Fig. 3).

Additional spots, half way between the MgO Bragg beams, are visible only in the pattern from the MR films (Fig 8b), providing the first evidence for presence of a cubic iron oxide structure that could provide an explanation for the measured ferromagnetic properties. Both Fe_3O_4 and γ-Fe_2O_3 are ferrimagnetic and have unit cells close to double in size of the MgO unit cell. Detailed lattice spacing measurements from SAD patterns confirm that the structure of the interfacial band in the MRc samples is consistent with Fe_3O_4 growing with its (111) planes parallel to the substrate and film surface in simple cube-on-cube orientation relationship with MgO. The Fe_3O_4 phase was not seen by RHEED, indicating that it is absent at the film surface. Upon detecting it with the strongly scattering high-energy electrons in transmission, it is possible to discern a very noisy broad peak at the position for the cubic (333) (Fe_3O_4 or γ-Fe_2O_3) Bragg reflection in the MR film (Fig. 3), suggesting that the magnetic phase constitutes a small fraction of the entire iron-oxide film volume. We next employ TEM and HRTEM to find the location of

the magnetic phase, and position-resolved EELS to compare its composition to that of the dominant hematite phase.

Figure 9 shows cross-sectional HTREM images (top) from the interface regions of films grown on magnesia and numerical diffractograms (bottom: shown with reversed contrast) from selected image regions. The interface appears straight and fairly abrupt in both cases, but in the MUc film (Fig. 9a) the hexagonal hematite structure initiates at the interface and propagates throughout the film. In contrast, the MRc film (Fig. 9b) initiates with an interfacial cubic phase and then transforms abruptly into the dominant hexagonal (hematite) phase, as confirmed by the indexed numerical Fourier transforms (Fig 9c) of the MgO substrate, Fe_3O_4 interfacial band and α-Fe_2O_3 film regions. Table 3 summarizes the experimentally measured lattice spacing and inter-planar angle values and compares them to the relevant iron oxide bulk standards. Cubic γ-Fe_2O_3 has similar lattice parameters as Fe_3O_4, but with additional allowed 1-10, 3-30, 201 reflections that fall within the resolution limits of the microscope. Such maghemite specific reflections were not observed in our experimental SAD and FFT patterns (as denoted by the dotted red unit cell with empty red squares). We also did not detect Fe metal and FeO lattice spacings.

Recent electron diffraction studies have reported Ar^+ sputtering-induced reduction of geological hematite single crystals with creation of subsurface spinel layers, but the effect was not observed in hematite crystals that are impurity free [41]. In our extended HRTEM imaging and SAD diffraction studies of samples milled with different Ar^+ energies, and under different angles of incidence, we have found evidence for sputtering-induced surface reduction of the ultra-pure OPA-MBE created hematite not only to defective epitaxial spinel, but also to rock salt surface layers upon excessive milling. This phenomenon contributes faint reflections in the FFT patterns from hematite film regions (denoted with squares in the right panel in Fig. 9c) where the

sputtering results in reduction of the top and bottom ion-milled surfaces through which the electron beam passes as it enters and exits the hematite film. Double diffraction of the magnetite {3-11} reflections by the hematite {0-11-2} planes results in ½ (01-12) reflections that are kinematicaly forbidden. The sputtering-induced magnetite reflections and their associated ½ (01-12) double diffraction reflections are visible only from the extremely thin specimen areas, such as those needed for phase contrast lattice imaging, when the damaged entry and exit layers encompass sizable fraction of the total electron beam propagation length. These reflections are negligible in thicker specimen regions, such as those used for the SAD patterns in figure 8, where the interfacial magnetite band is observed only in the MR samples and not in the MU hematite samples milled under equivalent conditions. The self-assembled interfacial magnetite layer is substantially better ordered than the sputtering-induced surface magnetite layer. The hematite surface reduction was found to be minimized when sputtering is performed with low energy (300 -500 eV) Ar ions at very low grazing angles of incidence (1-3 degrees), without affecting the thickness of the interfacial magnetite band.

The digital diffractograms of start-stop film MRs was also found to contain an interfacial magnetite band, but of a smaller thickness (1.63± 0.19 nm) compared to the MRc film (6.25 ± 0.12 nm). This is likely due to the difference in their substrate surface terminations, with dominance of the (2×2) reflections in MRs and ($\sqrt{3}\times\sqrt{3}$)R30° reflections in MRc,. The mode of growth (continuous vs. start-stop), and temperature gradients across the substrate might have also contributed to the differences in the local width of the interfacial magnetite band, as well as the ultimate film thickness that is finally achieved. Nevertheless, by comparison to the MU films, the interfacial magnetite band is clearly related to the surface reconstruction of the substrate. The hematite film grown on unreconstructed alumina does not contain interfacial bands of different

structure, but it hosts a periodic network of misfit dislocations as reported in prior HRTEM studies [38].

HRTEM studies of the middle and top regions of all films find them to be single-phase hematite, confirming that the main differences in structure occur at the interface during the initial stages of growth. This observation of interfacial magnetite bands in films grown on the reconstruction stabilized polar magnesia surface explains why they have markedly higher coercivity and saturation magnetization than the films grown on unreconstructed (hydrogen stabilized) polar magnesia and alumina surfaces.

Position resolved EELS studies of cross sectional samples were undertaken to probe the composition of the interface band seen in the hematite films grown on the reconstruction-stabilized magnesia surfaces. The EELS spectra shown in Fig. 10 are recorded with an electron probe of ~2 nm in diameter positioned on representative film (a) and interfacial (b) regions of sample MRc. The Fe L_3/L_2 ratios obtained from the background corrected spectra show a marked difference, indicative of changed oxidation states [42,43]. The experimental ratio for the Fe_2O_3 of 4.6 is in agreement with literature values [42]. The ratio at the interface is significantly lower and close to the value measure for Fe_3O_4 [42]. The lower oxidation state of Fe measured for the interface is confirmed by a the larger FWHM of the L_3 peak: 3.9eV for the Fe_2O_3 film and 4.5eV for the interface region. All EELS results indicate that the interface iron oxide has markedly lower oxidation state than the remainder of the film, conclusively proving that this cubic structure is Fe_3O_4, not γ-Fe_2O_3.

Interfacial bands with different phase composition have been detected in many *in-situ* studies during the initial stages of growth, but most are of a transient nature. These "ghost" phases disappear as the film grows, and cannot be detected with post-deposition characterization

methods that are sensitive to buried interfacial films, unlike the "real" magnetite interface band observed in this work when hematite is grown on the reconstructed magnesia polar surface. For example, extensive systematic studies of epitaxial hematite growth on single crystal Pt(111) surfaces, have shown complex "ghost" phase behavior: FeO(111) forms as an initial transient phase (≤2.5ML), transforming into Fe_3O_4(111) for continued growth (at 870 K or 1000 K), and into hematite by oxidative post annealing (1000K;10^{-1} mbar O_2) [40]. Using the same metal substrate, OPA-MBE studies have found transient γ-Fe_2O_3(111) that grows in a layer-by-layer mode up to ~2 nm and in island mode up to ~3 nm, then transforms into α-Fe_2O_3(0001) and continues to grow in columnar mode [44]. These morphological and structural transformations were correlated with ferrimagnetic to antiferromagnetic transition and progressive structural relaxation.

Hematite growth on lattice-matched oxides is even more complex. Comparative OPA-MBE studies on alumina and neutral magnesia surfaces have found that α-Fe_2O_3(0001) grows on α-Al_2O_3(0001) [45], but cubic γ-Fe_2O_3(001) forms on MgO(001) [23, 45]. In-situ structural studies have uncovered transient γ-Fe_2O_3 [39] or 2ML of FeO phase [46] in the initial stages of OPA- or atomic oxygen assisted (OA)-MBE hematite growth on alumina. By switching from the neutral (001) to the polar (111) magnesia surface, the present work demonstrates that α-Fe_2O_3(0001) can be grown on the polar face of a cubic MgO crystal, both as a virtually pure phase on the unreconstructed surface, and with an Fe_3O_4(111) interfacial band on the reconstructed MgO(111) surface. It remains to be explored if "ghost" phases form during hematite growth on the unreconstructed MgO(111) surface.

Referring back to the bulk atomic models in Figure 1, it is not surprising that we can grow a hexagonal corundum structure on a cubic rock-salt structure, considering the nearly

prefect match between their oxygen sub-lattices, and the hexagonal in-plane symmetry of the close-packed Mg and O (111) planes that is maintained in the MgO(111)-(1×1)-OH termination. The same logic could be used to argue that the interfacial Fe_3O_4(111) forms because it provides the correct lattice orientation and a better lattice match to a reconstructed MgO(111)-(2×2) surface. However, this elastic constraint argument fails to explain why we see an interfacial band of magnetite on the MgO(111)-($\sqrt{3}\times\sqrt{3}$)R30° reconstructed surface that is ideally oriented for the growth of the hematite lattice. Moreover, the elastic constraint argument cannot provide an explanation for the lower oxidation state of the self-assembled interfacial Fe_3O_4 layers, especially when γ-Fe_2O_3 would provide the same elastic relief as magnetite while keeping the same oxidation state as hematite. Therefore, we believe that our experimental results can only be understood within the polarity hypothesis framework presented in the introduction.

D. Discussion

The most surprising and significant finding of this study is the dependence of the hematite film morphology, atomic structure, and transport properties on the polar magnesia stabilization mechanism. The simplest explanation for the observed differences is provided by the discovery of interfacial magnetite bands in hematite films grown on reconstructed magnesia surfaces. Such a magnetite layer can act as a structural buffer, providing better lattice match with the substrate and hence a smoother film surface morphology. Its presence also explains the mixed ferri/antiferromagnetic film properties. This buffer layer is not engineered by any of the customary external control mechanisms, but self-organizes to exclude incorporation of oxygen even under (strongly oxidizing) kinetic and thermodynamic conditions designed for growth of hematite. Such expulsion of oxygen away from the polar interface is consistent with our previous observations of Fe nanoparticles at the interface of magnetite films grown by OPA-MBE on

unreconstructed MgO(111) [19] and Al_2O_3(0001) [23] surfaces. This behavior may also be explained by recent density functional theory predictions of outward motion of oxygen at hematite/magnesia interfaces [47]. Drastic structural relaxations were predicted at the interface, triggered by an expulsion of oxygen towards the surface and collapse of the interfacial Fe-bilayer in ultrathin films. The relaxed structure was found to consist of alternating planes of Fe_2-FeO_3, which is a non-bulk iron oxide phase. Such behavior was not observed in model calculations of hematite films on metallic Ti(0001) and Al_2O_3(0001) substrates [48].

Returning back to the starting hypothesis it is reasonable to propose that this natural magnetite buffer self-assembles in response to the reconstructed-substrate polarity, providing a new compensation solution as the film growth starts to interfere and alter the stabilization mechanism of the bare polar oxide surface. This hypothesis is further supported by the observation that the magnetite buffer self-assembles on the reconstruction-stabilized magnesia surfaces, but not on the hydrogen-stabilized unreconstructed surfaces. Hydrogen has also been shown to stabilize the unreconstructed (0001) alumina surfaces and affect the initial stages of growth by promoting laminar growth in place of the usual island growth of ultrathin Co films [49]. It remains to be determined if this natural magnetite buffer will form when hematite is grown on other reconstruction-stabilized polar surfaces, or even on the hydrogen stabilized 1x1 surfaces under less over-engineered kinetic and thermodynamic conditions. It is also unknown at this time how this polarity-induced self-assembled buffer compares to conventional buffers in its detailed structural and electronic properties.

This study also demonstrated that hematite films can be grown on the (1×1) terminated MgO(111), as has been achieved previously on Al_2O_3(0001) surfaces. While both types of hematite films have antiferromagnetic macroscopic properties, their short range spin ordering

differs, as revealed by our XMCD studies. These changes in the local crystal field of the Fe^{3+} ion could be attributed to magnetoelastic interactions that are further affected by differences in local strain relaxation around defect structures. Indirect evidence for this phenomenon is provided by experiments that show thickness dependent magnetic properties, including the absence of a Morin transformation, for ultra-thin (2 nm and 8 nm) α-Fe_2O_3 films on Al_2O_3(0001) [50]. In addition to finite size effects, changes in the local crystal field of the Fe^{3+} ion, and magnetoelastic interactions, it is plausible that the difference in polarity between MgO(111) and Al_2O_3(0001) further contributes to the difference in the hematite magnetic ordering. Our detailed theoretical study on the growth of thin hematite films on polar MgO(111) and unsupported hematite(0001) slabs, showed the presence of metastable magnetic states in both cases [47]. Further theoretical modeling is under way to explore the magnetic ordering in hematite films grown on Al_2O_3(0001) substrates.

Conclusions

This study shows that different modes of polar surface stabilization can have profound effect on the growth mode, phase composition, and magnetic properties of polar hematite films grown on polar magnesia and alumina single crystal substrates. Growth on reconstruction-stabilized magnesia results in the formation of an interfacial band of magnetite, opening opportunities to create novel magnetic hetero-structures. This self-organized magnetite buffer persists after growth, in contrast to the transient maghemite detected by recent *in-situ* studies during early stages growth on unreconstructed alumina surfaces. Indeed, virtually pure phase α-Fe_2O_3(0001) is obtained on the hydrogen-stabilized unreconstructed MgO(111) and α-

Al_2O_3(0001) surfaces, with antiferromagnetic macroscopic properties, but with differences in the microscopic defect structure and spin ordering.

Acknowledgments

This work is supported by the Department of Energy under grant number DE-FG02-06ER46328. Film growth, surface structure, and magnetic studies were performed at the Environmental Molecular Sciences Laboratory, a national scientific user facility sponsored by the Department of Energy's Office of Biological and Environmental Research, located at Pacific Northwest National Laboratory. Interface structural studies were performed in the Laboratory for High Resolution Electron Microscopy at the University of Wisconsin-Milwaukee, with technical assistance by D. P. Robertson, and valuable discussions with M. A. Schofield. Work at Argonne National Laboratory is supported by the U. S. Department of Energy, Office of Science, Office of Basic Energy Sciences, under Contract No. DE-AC02-06CH11357.

References

1. P. W. Tasker, J. Phys. C: Solid State Phys. **12**, 4977 (1979).
2. V. E. Henrich and P. A. Cox, *The Surface Science of Metal Oxides*, Cambridge University Press, Cambridge/New York, 1994.
3. C. Noguera, Physics and Chemistry at Oxide Surfaces, Cambridge University Press, Cambridge/New York, 1996.
4. C. Noguera, J. Phys.: Condens. Matter **12**, R367 (2000).
5. M. Gajdardziska-Josifovska, R. Plass, M. A. Schofield, D. R. Giese, and R. Sharma, J. Electron Micr. **51**, S13 (2002).
6. J. Goniakowski, F. Finocchi, and C. Noguera, Rep. Prog. Phys. **71**, 16501 (2008).
7. M. Gajdardziska-Josifovska, P. A. Crozier, and J. M. Cowley, Surf. Sci. Lett. **248**, L259 (1991).
8. D. Wolf, Phys. Rev. Lett. **68**, 3315 (1992).
9. A. Pojani, F. Finocchi, J. Goniakowski and C. Noguera, Surf. Sci. **387,** 354 (1997).
10. R. Plass, K. Egan, C. Collazo-Davila, D. Grozea, E. Landree, L. D. Marks, and M.Gajdardziska-Josifovska, Phys. Rev. Lett. **81**, 4891 (1998).
11. A. Subramanian, L. D. Marks, O. Warschkow, and D. E. Ellis, Phys. Rev. Lett. **92**, 026101 (2004).
12. F. Finocchi, A. Barbier, J. Jupille, and C. Noguera, Phys. Rev. Lett. **92**, 136101 (2004).
13. J. Ciston, A. Subramanian, and L. D. Marks, Phys Rev B 79, 085421 (2009).

14. K. Refson, R. A. Wogelius, D. G. Fraser, M. C. Payne, M. H. Lee, and V. Milman, Phys. Rev. B **52**, 10823 (1995).

15. A. Wander, I. J. Nush, and N. M. Harrison, Phys. Rev. B **68,** 233405 (2003).

16. V. K. Lazarov, R. Plass, H-C. Poon, D. K. Saldin, M. Weinert, S. A. Chambers, and M. Gajdardziska-Josifovska, Phys. Rev. B **71**, 115434 (2005).

17. H-C. Poon, X. F. Hu, S E Chamberlin, D. K. Saldin, and C. J. Hirschmugl, Surf. Sci. **600**, 2505 (2006).

18. V. K. Lazarov, S.A. Chambers, and M. Gajdardziska-Josifovska, Phys. Rev. Lett. **90,** 216108 (2003).

19. V. K. Lazarov, M. Weinert, S.A. Chambers, and M. Gajdardziska-Josifovska, Phys. Rev. B **72**, 195401 (2005).

20. S. A. Chambers, S. Thevuthasan, and S. Joyce, Surf. Sci. **450**, L273 (2000).

21. B. Stanka, W. Hebenstreit, U. Diebold, and S. A. Chambers, Surf. Sci. **448**, 49 (2000).

22. W. Weiss, A. Barbieri, M. A. Van Hove, and G. A. Samorjai, Phys. Rev. Lett. **71**, 1848 (1993).

23. R. F. C. Farrow, P. M. Rice, M. F. Toney, R. F. Marks, J. A. Hedstrom, R. Stephenson, M. J. Carey, and A. J. Kellock, J. Appl. Phys. **93**, 5626 (2003).

24. V. K. Lazarov, J. Zimmermann, S. H. Cheung, L. Li, M. Weinert, and M. Gajdardziska-Josifovska, Phys. Rev. Lett. **94**, 216101 (2005).

25. W. Weiss and W. Ranke, Prog. Surf. Sci. **70**, 1 (2002).

26. S.A. Chambers, Surf. Sci. Rep. **39**, 105 (2000).

27. U Diebold, SC Li and M. Schmid, Ann. Rev. Phys. Chem. 61, 129 (2010)

28. E. Vescovo, H.-J.Kim, J.M. Ablett, and S.A. Chambers, J. Appl. Phys. **98**, 084507 (2005).

29. J.G. Tobin, S.A. Morton, S.W. Yu, G.D. Waddill, I.K. Schuller, and S.A. Chambers, J. Phys: Cond. Mat. **19**, 315218 (2007).

30. J. S. Moodera, L. R. Kinder, T. M. Wong, and R. Meservey, Phys. Rev. Lett. **74**, 3273 (1995).

31. I. Cesar, A. Kay, J. A. Gonzales Martinez, and M. Gratzel, J. Am. Chem. Soc. **128**, 4582 (2006).

32. R. M. Cornell and U. Schwertmann, The Iron Oxides, Wiley-VCH, (1997).

33. F. C. Voogt, T. Hibma, G. L. Zhang, M. Hoefman, and L. Niesen, Surf. Sci. **331–333**, 1508 (1995).

34. W. F. J. Fontijn, R. M. Wolf, R. Metselaar, and P. J. van der Zaag, Thin Solid Films **292**, 270 (1997).

35. F. C. Voogt, T. Hibma, P. Smulders, and L. Niesen, J.Cryst. Growth **174**, 440 (1997).

36. Y. Gao, Y. J. Kim, S. Thevuthasan, S. A. Chambers, and P. Lubitz, J. Appl. Phys. **81**, 3253 (1997).

37. T. Fujii, D. Alders, F. C. Voogt, T. Hibma, B. T. Thole, and G. A. Sawatzky, Surf. Sci. **366**, 579 (1996).

38. C. M. Wang, S. Thevuthasan, F. Gao, D. E. McCready, and S. A. Chambers, Thin Solid Films **414,** 31 (2002).

39. I. J. Lee, J-K Lim, C. Yu, C-H Chang, M-K Joo, Y-P Lee, T-B Hur and H-K Kim, J. Vac. Sci. Technol. A **23**, 1450 (2005).

40. W. Weiss and M. Ritter, Phys. Rev. B **59**, 5201 (1999).

41. A. N. Chiaramonti, P. C. Stair, and L. D. Marks, Surf. Sci. **586**, 38 (2005).

42. C. Colliex, T. Manoubi, and C. Ortiz, Phys. Rev. B **44**, 11402 (1991).

43. L. Cave, T. Al, D. Loomer, S. Cogswell, and L. Weaver, Micron **37**, 301 (2006).

44. A. Barbier, R. Belkhou, P. Ohresser, M. Gautier-Soyer, O. Bezencenet, M. Mulazzi, M.-J. Guittet, and J.-B. Moussy, Phys. Rev. B **72**, 245423 (2005).

45. J. Kim, Y. Gao, and S. A. Chambers, Surf Sci. **371**, 358 (1997).

46. S. Gota, E. Guiot, M. Henriot, and M. Gautier-Soyer, Phys. Rev. B **60**, 14387 (1999).

47. K. Pande, M. Gajdardziska-Josifovska and M. Weinert, (unpublished)

48. K. Pande, M. Gajdardziska-Josifovska and M. Weinert, (unpublished)

49. S.A. Chambers, T. Drubay, D.R. Jennison, and T.R. Mattsson, Science **297**, 827 (2002).

50. S. Gota, M. Gautier-Soyer, and M. Sacchi, Phys. Rev. B **64**, 224407 (2001).

Table 1. Summary of substrate surface structure and deposition conditions for five films grown under identical iron flux (~0.01 nm/s), oxygen partial pressure (~$2x10^{-5}$ torr), and substrate temperature (~400°C), on unreconstructed (U) and reconstructed (R) magnesia (M) and alumina (A) single crystals in continuous (c) or start-stop (s) fashion.

Sample	Substrate Surface	Deposition Time (min)	Nominal Film Thickness (nm)
MUc	MgO(111)-(1×1)	172	200
MUs	MgO(111)-(1×1)	12+108	180
AUc	Al_2O_3(0001)-(1×1)	180	200
MRc	MgO(111)-(√3×√3)R30°&(2×2) (√3×√3)R30° dominant	70	80
MRs	MgO(111)-(√3×√3)R30°&(2×2) (2×2) dominant	17+80+82	200

Table 2. Magnetic properties for hematite films from Table 1: M_s – saturation magnetization at external field of 1T; M_r – remanence magnetization; H_c – coercivity; H_{cr} – magnetic field needed to remove remanence.

Sample	M_s (10^{-6} Am^2)	M_r/M_s	H_c (10^{-4} T)	H_{cr}/H_c	M_s/ thickness (10^3 Am)	Interfacial band
MUc	305	0.195	106	2.73	2.72	No
AUc	330	0.425	388	2.58	1.65	No
MRc	1173	0.326	338	1.90	16.76	Yes

Table 3. Results from lattice spacing and inter-planar angle measurements utilizing experimental numerical diffractograms (Fig. 9c) from HRTEM image regions of sample MRc (Fig. 9b). Phase identification of magnetite interfacial band and hematite film is obtained by comparison with bulk spacing and angles of iron oxides.

h k l	Spacing (nm)	Angle (deg)	Bulk Spacing (nm)	Bulk Angle (deg)
Substrate: MgO(111) in [11-2] zone				
2-2 0	0.147	0	0.1488	0.0
1 1 1	0.242	89	0.2431	90.0
Interfacial Band: Fe_3O_4 (111) in [11-2] zone				
2-2 0	0.297	0	0.2967	0.0
4-4 0	0.149	1	0.1485	0.0
1 1 1	0.496	90	0.4852	90.0
2 2 2	0.242	90	0.2424	90.0
3-1 1	0.252	32	0.2532	31.5
6-2 2	0.127	31	0.1266	31.5
Film: α-Fe_2O_3(0001) in [2-1-10] zone				
0 3-3 0	0.144	0	0.1452	0.0
0 0 0 6	0.233	89	0.2285	90.0
0 1-1 2	0.366	32	0.3660	32.4
0-1 1 4	0.271	128	0.2690	122.4
0 3-3 6	0.183	32	0.1226	32.4

Figure Captions

Figure 1 (color online): Atomic models in side and top view of (a) α-Fe_2O_3(0001) – corundum (also α-Al_2O_3), (b) Fe_3O_4(111) – spinel, and (c) MgO(111) – rocksalt slabs with bulk terminated polar surfaces. The side view illustrates alternate stacking of planes of oxygen anions (O^{2-} in green) and magnesium (Mg^{2+}, orange) or iron (Fe^{3+} and Fe^{2+}, purple) cations needed for polar oxide surface and/or interface creation. In all (111) cubic planes and in the α-Al_2O_3 (0001) hexagonal planes the O^{2-} ions are in a close-packed hexagonal lattice, with in-plane distortions from the perfect lattice sites for hematite (0001) planes. Iron (aluminum) is stacked in bilayers of Fe^{3+} (Al^{3+}) in the α-Fe_2O_3 (α-Al_2O_3) polar (0001) direction, and in alternating monolayers of Fe^{3+} and trilayers of $Fe^{2+}Fe^{3+}Fe^{2+}$ in the Fe_3O_4 polar (111) direction. Top view drawings of the unreconstructed surface unit cells for all three structures illustrates that the α-Fe_2O_3(0001)-(1×1) cell is nearly commensurate with MgO(111)-(√3×√3)R30° and Fe_3O_4(111)-(1×1) with MgO(111)-(2×2).

Figure 2 (color online): Thickness normalized VSM magnetization curves for films grown on magnesia and alumina polar surfaces in continuous fashion. Saturation moment and coercivity data are presented in Table 2 with drastically higher magnetic moment for the film grown on reconstructed magnesia (MR).

Figure 3 (color online): XRD intensity profiles of iron oxide films grown in continuous mode on unreconstructed (MUc) and reconstructed (MRc) MgO(111) surfaces displaying hematite reflections in α-Fe_2O_3 (0001) epitaxial orientation. Lines indicate peak positions for magnesia, hematite, magnetite and maghemite.

Figure 4 (color online): Fe L (a) and O K (b) XAS and Fe L XMCD (a) spectra of hematite films grown by continuous OPA-MBE deposition on hydrogen-stabilized MgO(111) and Al_2O_3(0001) unreconstructed surfaces (MUc, AUc) and on reconstruction-stabilized MgO(111) polar surfaces (MRc).

Figure 5 (color online): *In situ* Fe 2p XPS spectra from hematite films grown by continuous OPA-MBE on unreconstructed (MU) and reconstructed (MR) MgO(111) and unreconstructed (AU) Al_2O_3 (0001) polar surfaces. Dashed lines denote positions of Fe^{3+} peaks in close agreement with bulk Fe_2O_3 values of 711 eV for Fe $2p_{3/2}$ and 719 eV for the satellite.

Figure 6 (color online): In-situ RHEED patterns from magnesia and alumina substrates after surface preparation for growth (top row) and from respective hematite film surfaces after completion of the OPA-MBE growth (bottom row): a) MUc film on unreconstructed MgO(111) substrate; b) MRc film on reconstructed MgO(111)-($\sqrt{3}\times\sqrt{3}$)R30° with minority (2×2) domains; and c) AUc film on unreconstructed Al_2O_3(0001) surface. d) RHEED in-plane intensity profiles of above films are consistent with α-Fe_2O_3(0001)-(1×1) termination structure. The rods and their intensity profiles are indexed; arrows in patterns denote location of magnesia (green), alumina (blue), and hematite (orange) reflections, lines of same color indicate the substrate 1×1 rods.

Figure 7 (color online): Bright-field TEM image of MUc film, imaged in cross section under weakly diffracting conditions, allows measurement of film thickness and ascertains absence of dense Fe nanoparticles.

Figure 8 (color online): Selected area diffraction patterns from films grown on a) unreconstructed (MUc) and b) reconstructed (MRc) magnesia surfaces recorded with the incident beam parallel to MgO [11-2] direction. The hematite (orange) and magnesia (green) unit cells are denoted on the experimental patters, showing that additional reflections, due to magnetite (lilac), are present only in the MRc sample.

Figure 9 (color online): HRTEM images of interface regions of MUc (a) and MRc (b) samples and indexed digital diffractograms (c) from MgO substrate (green), Fe_3O_4 interfacial band (lilac), and α-Fe_2O_3 film (orange) image regions. The self-assembled interfacial nanobuffer with magnetite structure is seen in the films grown on reconstructed MgO(111). Cubic γ-Fe_2O_3 is not present, as demonstrated by absence of 1-10 and 201 reflections (red).

Figure 10: Position resolved EELS spectra of the Fe – L transition from: a) hematite regions of film MRc; and b) interfacial magnetite-like band of the same film grown on reconstruction-stabilized MgO(111)-($\sqrt{3}\times\sqrt{3}$)R30° polar surfaces. The grey area was subtracted prior to L_3/L_2 calculation. The L_3/L_2 ratio and the FWHM values of the L_3 peak indicate a lower Fe oxidation state at the interface. Background subtracted spectra.

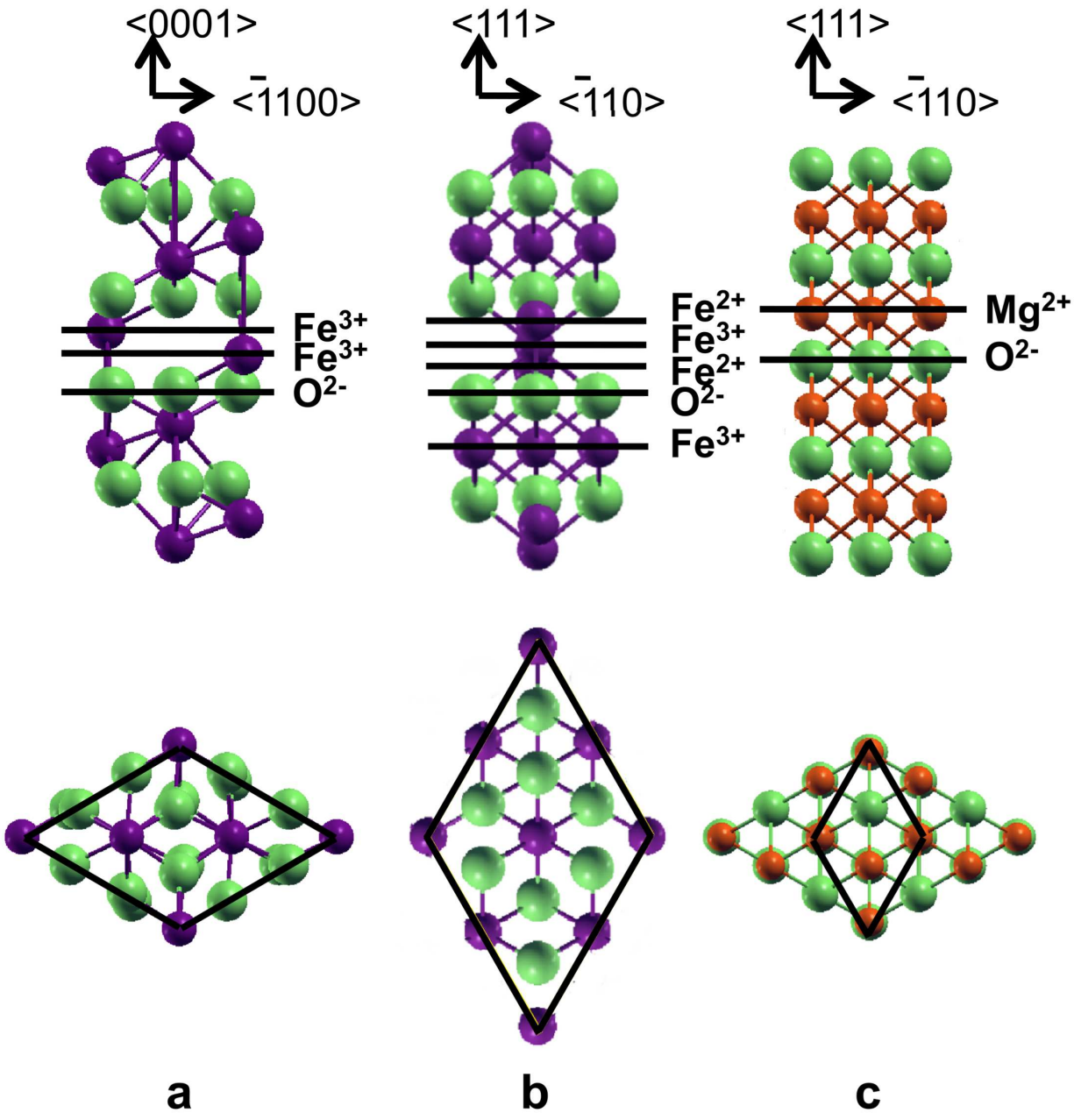

Figure 1 BT10699 21NOV2011

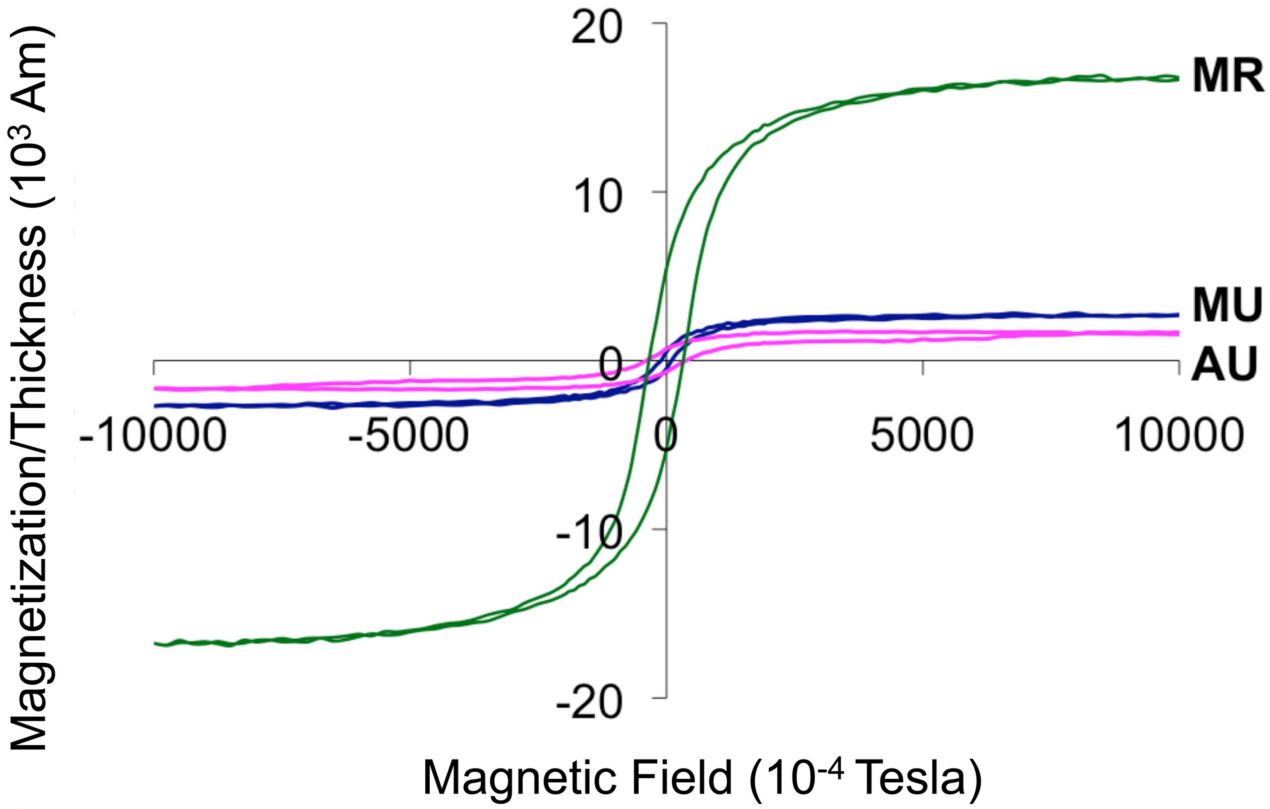

Figure 2 BT10699 21NOV2011

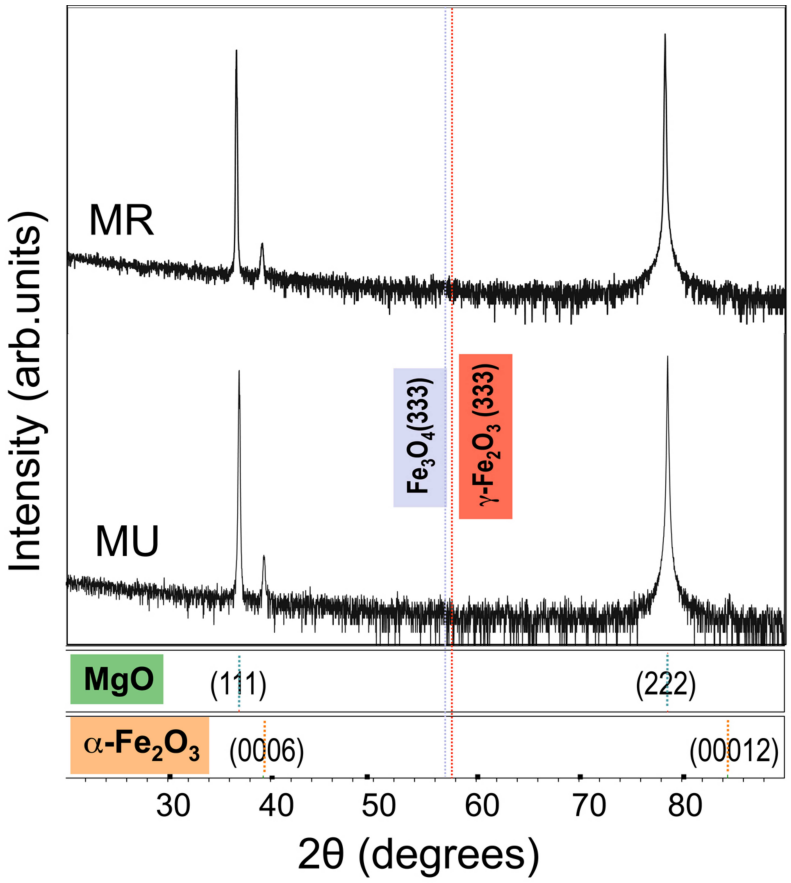

Figure 3 BT10699 21NOV2011

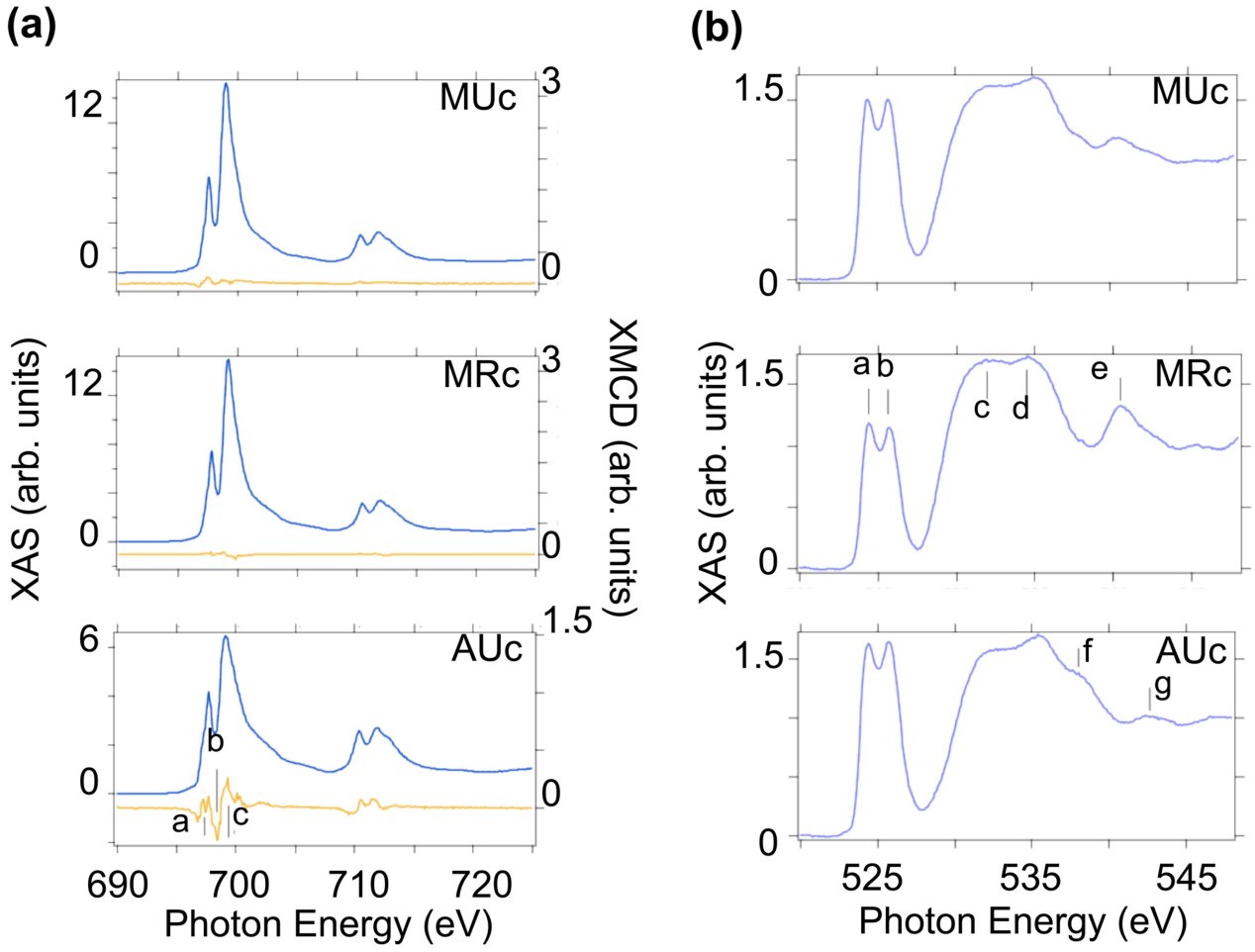

Figure 4 BT10699 21NOV2011

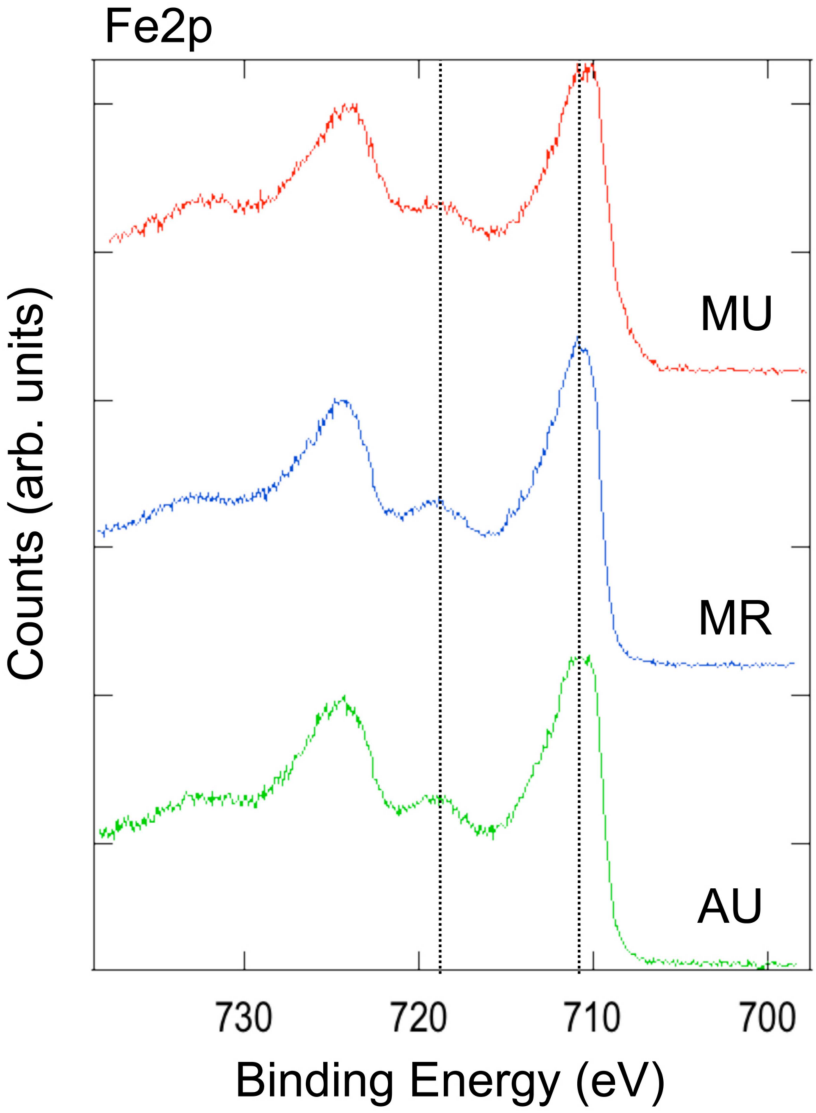

Figure 5 BT10699 21NOV2011

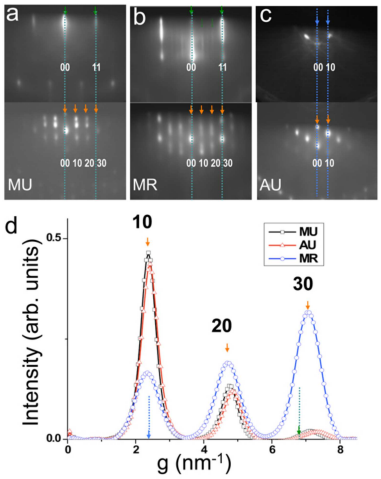

Figure 6 BT10699 21NOV2011

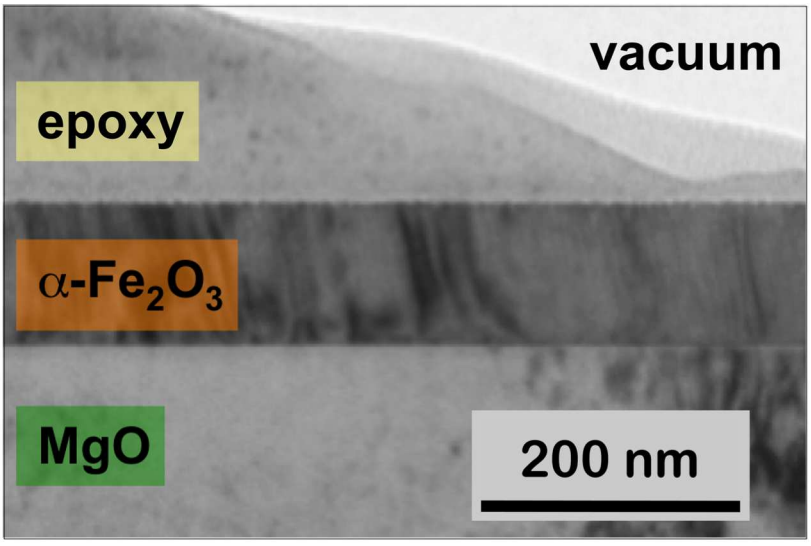

Figure 7 BT10699 21NOV2011

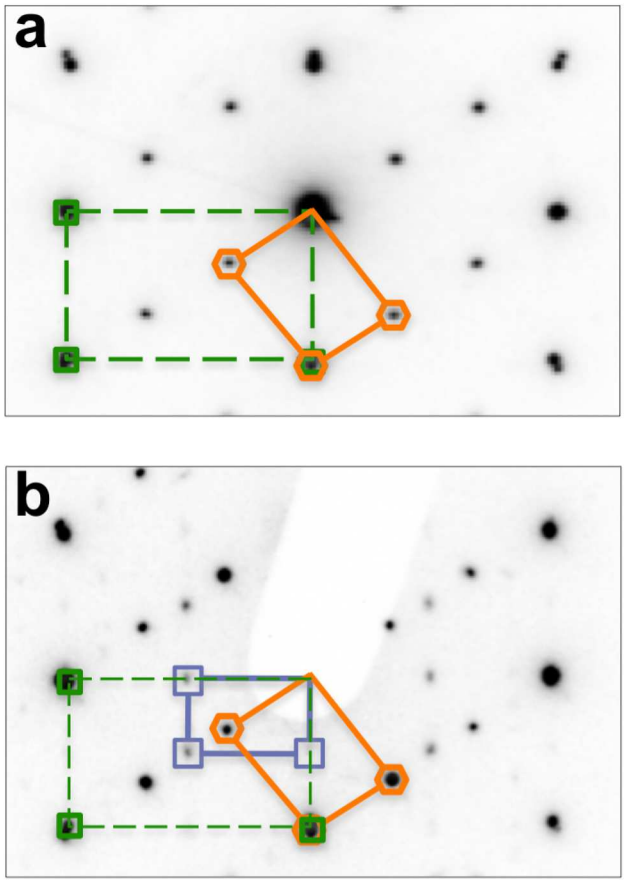

Figure 8 BT10699 21NOV2011

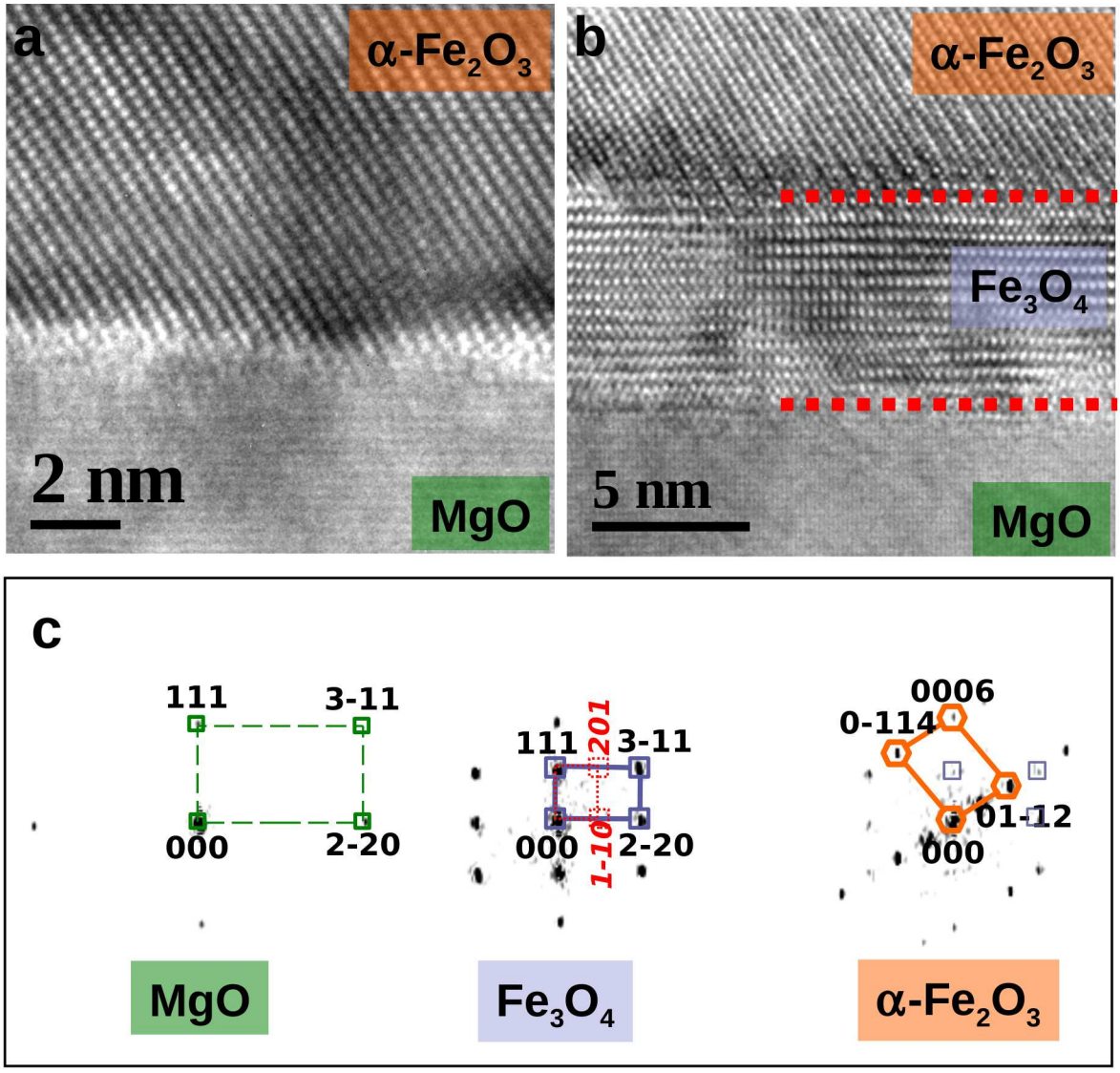

Figure 9 BT10699 21NOV2011

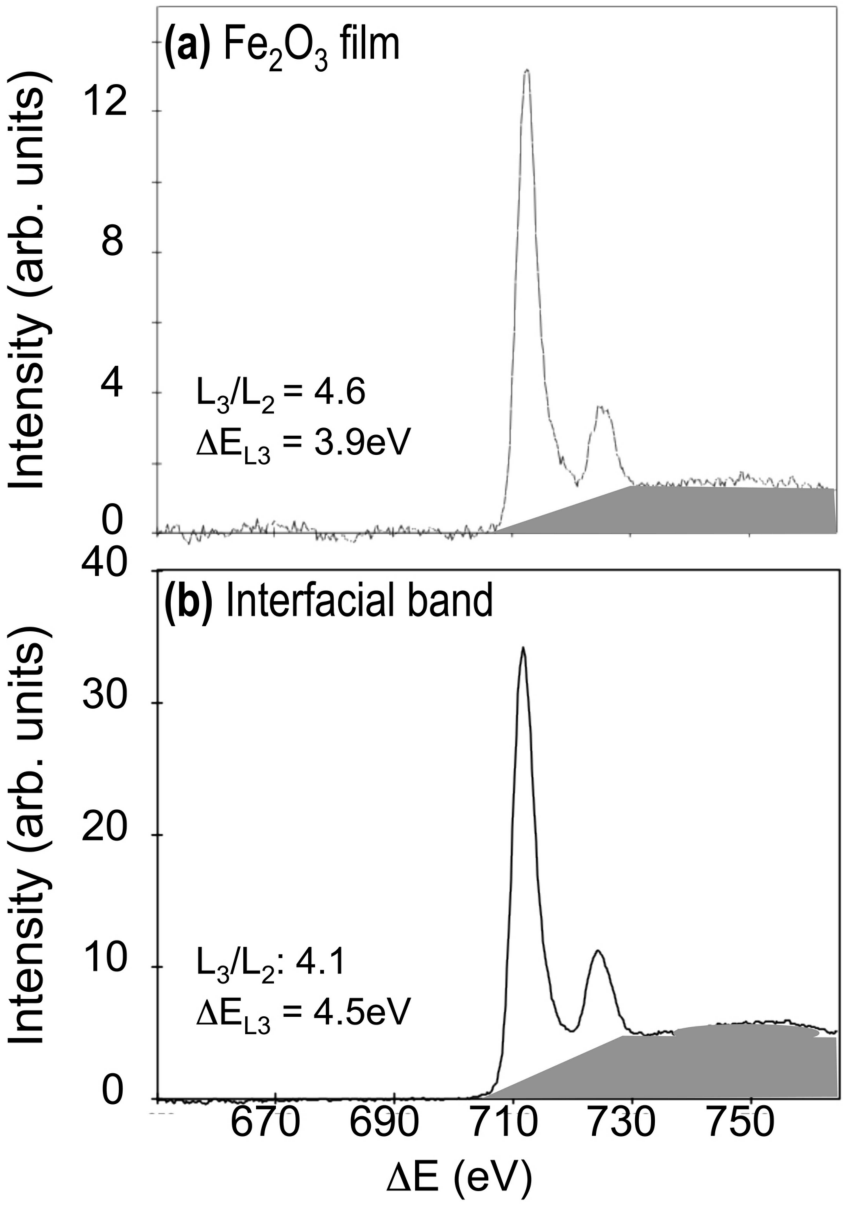

Figure 10 BT10699 21NOV2011